



**HAL**  
open science

## Structure and Formation Kinetics of Millimeter-Size Single Domain Supercrystals

Daniel García-Lojo, Evgeny Modin, Sergio Gómez-Graña, Marianne Impéror, Andrey Chuvilin, Isabel Pastoriza-santos, Jorge Pérez-juste, Doru Constantin, Cyrille Hamon

► **To cite this version:**

Daniel García-Lojo, Evgeny Modin, Sergio Gómez-Graña, Marianne Impéror, Andrey Chuvilin, et al.. Structure and Formation Kinetics of Millimeter-Size Single Domain Supercrystals. *Advanced Functional Materials*, 2021, pp.2101869. 10.1002/adfm.202101869 . hal-03210614

**HAL Id: hal-03210614**

**<https://hal.science/hal-03210614v1>**

Submitted on 28 Apr 2021

**HAL** is a multi-disciplinary open access archive for the deposit and dissemination of scientific research documents, whether they are published or not. The documents may come from teaching and research institutions in France or abroad, or from public or private research centers.

L'archive ouverte pluridisciplinaire **HAL**, est destinée au dépôt et à la diffusion de documents scientifiques de niveau recherche, publiés ou non, émanant des établissements d'enseignement et de recherche français ou étrangers, des laboratoires publics ou privés.

# Structure and Formation Kinetics of Millimeter-Size Single Domain Supercrystals

Daniel García-Lojo,<sup>1,2</sup> Evgeny Modin,<sup>3</sup> Sergio Gómez-Graña,<sup>1,2</sup> Marianne Impéror-Clerc,<sup>4</sup> Andrey Chuvilin,<sup>3,5</sup> Isabel Pastoriza-Santos,<sup>1,2</sup> Jorge Pérez-Juste,<sup>1,2\*</sup> Doru Constantin,<sup>4\*</sup> Cyrille Hamon<sup>4\*</sup>

<sup>1</sup> CINBIO, Universidade de Vigo, Departamento de Química Física, Campus Universitario As Lagoas, Marcosende, 36310 Vigo, Spain.

<sup>2</sup> Galicia Sur Health Research Institute (IIS Galicia Sur), SERGAS-UVIGO, 36310 Vigo, Spain.

<sup>3</sup> Electron Microscopy Laboratory, CIC NanoGUNE BRTA, Tolosa Hiribidea, 76, 20019 Donostia – San Sebastian, Spain.

<sup>4</sup> Université Paris-Saclay, CNRS, Laboratoire de Physique des Solides, 91405 Orsay, France.

<sup>5</sup> Basque Foundation of Science, IKERBASQUE, 48013 Bilbao, Spain.

\* Corresponding authors

Jorge Pérez-Juste: [juste@uvigo.es](mailto:juste@uvigo.es)

Doru Constantin : [doru.constantin@universite-paris-saclay.fr](mailto:doru.constantin@universite-paris-saclay.fr)

Cyrille Hamon: [cyrille.hamon@universite-paris-saclay.fr](mailto:cyrille.hamon@universite-paris-saclay.fr)

KEYWORDS: Supercrystal, time resolved-SAXS, Microfluidic self-assembly, FIB-SEM tomography.

## **Abstract**

Organizing nanoparticles (NPs) into periodic structures is a central goal in materials science. Despite progress in the last decades, it is still challenging to produce macroscopic assemblies reliably. In this work, we report the analysis of the pervaporation-induced organization of gold octahedra into supercrystals within microfluidic channels using a combination of X-ray scattering techniques and FIB-SEM tomography. The results reveal the formation of a single-domain supercrystal with a monoclinic  $C2/m$  symmetry and long-range order extending over the dimensions of the microfluidic channel, covering at least  $1.7 \times 0.3 \text{ mm}^2$ . Time-resolved small angle X-ray scattering analysis showed that the formation of the superlattice involves an accumulation of the NPs within the channel before the nucleation and growth of the supercrystal. The orientation of the crystal remains unchanged during its formation, suggesting a growth mechanism directed by the channel interface. Together, these results show the potential application of the pervaporation strategy to providing spatially determined control over NP crystallization, which can be used for the rational fabrication of nanomaterial architectures.

## Introduction

A central goal in nanoscience is creating extended periodic nanoparticle lattices to take advantage of new functionalities due to interparticle coupling.<sup>[1]</sup> Self-assembling nanoparticles (NPs) of various shapes (cuboctahedra, cubes, rhombic dodecahedra, octahedra and rods) by evaporation techniques has been used as a means to obtain different crystalline symmetries.<sup>[2]</sup> Among these shapes, the self-organization of octahedra has attracted particular attention because of the existence of several packing polymorphs within the samples. First examples were reported more than a decade ago, when the analysis of the structure of MnO<sup>[3]</sup> and Au<sup>[4]</sup> octahedra supercrystals revealed monoclinic and hexagonal lattices. Later, a dense Minkowski lattice was found in superlattices of Ag<sup>[2c, 5]</sup> and Au<sup>[6]</sup> octahedra. Although the Minkowski lattice is the densest structure and the preferred phase under high-pressure conditions, monoclinic and hexagonal lattices are frequently found within samples. Glotzer and Tang explained this phenomenon by the monoclinic lattice being entropically favored, while the hexagonal one has the highest contact fraction.<sup>[2c]</sup> In general, these types of structures were observed for assemblies of large (>30 nm) octahedra, while more open bcc lattices were found for smaller (<10 nm) octahedra of c-In<sub>2</sub>O<sub>3</sub>,<sup>[7]</sup> Pt<sub>3</sub>Ni,<sup>[8]</sup> Pt<sub>3</sub>Cu<sub>2</sub>.<sup>[9]</sup> This different behavior could be due to the nature of the interparticle interactions changing with particle size. In the case of small NPs, the interaction is driven not only by directional attractive forces (which result in facet alignment) but also by additional interactions due to the ligand shell, which might modify the symmetry of the supercrystal.<sup>[10]</sup> This polymorphism can act as a bottleneck for applications that need extended and uniform superlattices.

Various evaporation-induced self-assembly (EISA) techniques have been used to obtain supercrystals of octahedra. Controlled evaporation of a sessile drop was found to lead to different octahedra packing polymorphs<sup>[3-4]</sup> such as monoclinic and hexagonal lattices as well as the Minkowski lattice,<sup>[6]</sup> sometimes within the same sample. The formation of a Minkowski

lattice was observed in Ag<sup>[5]</sup> and Au<sup>[2c]</sup> octahedra supercrystals obtained by gravitational sedimentation.

Some techniques have demonstrated the possibility of assembling octahedra into superlattices over large length scales. For instance, monolayers of Ag octahedra self-assembled at a liquid/liquid interface into 2D sheets spanning several centimeters.<sup>[11]</sup> Faceted supercrystals of Au octahedra of tens of micrometers were obtained by EISA through a careful adjustment of surfactant concentration and temperature.<sup>[12]</sup> Pervaporation within a microfluidic channel also led to the hierarchical assembly of Au octahedra over millimeter scales.<sup>[13]</sup> These works were mainly focused on the synthesis and self-assembly of uniform Au octahedra without performing an exhaustive study of the formation and 3D packing arrangement of the NPs.

The pervaporation technique consists of evaporating the solvent through a permeable membrane, generating a solvent flux from the reservoir toward the channel, which drags the colloids into the end of the channel, leading to their accumulation and subsequent crystallization.<sup>[14]</sup> This technique can yield supercrystals with arbitrary morphology since the NP assembly adopts the microchannel shape and dimension.<sup>[13, 15]</sup> In the case of Au octahedra, the Scanning Electron Microscopy (SEM) analysis demonstrates the hierarchical organization of nanoparticles within the supercrystals,<sup>[13b, 15a]</sup> although the nanostructuration at large length scales or the crystal domain features were not elucidated. These analyses required the removal of the PDMS mold, which may result in partial damage or modification of supercrystal structure. Interestingly, the PDMS-based microfluidic platforms allow on-chip measurements by scattering techniques and therefore the complete characterization of the crystalline structure of the supercrystals. A microbeam Small Angle X-Ray Scattering (SAXS) analysis showed superlattices of gold spheres, but with a spatial extent limited to a few microns.<sup>[15a]</sup> Besides, over the last two decades, time-resolved SAXS has been used to investigate the formation of supercrystals in solution<sup>[16]</sup> or on substrates.<sup>[17]</sup> Technical constraints together with reduced

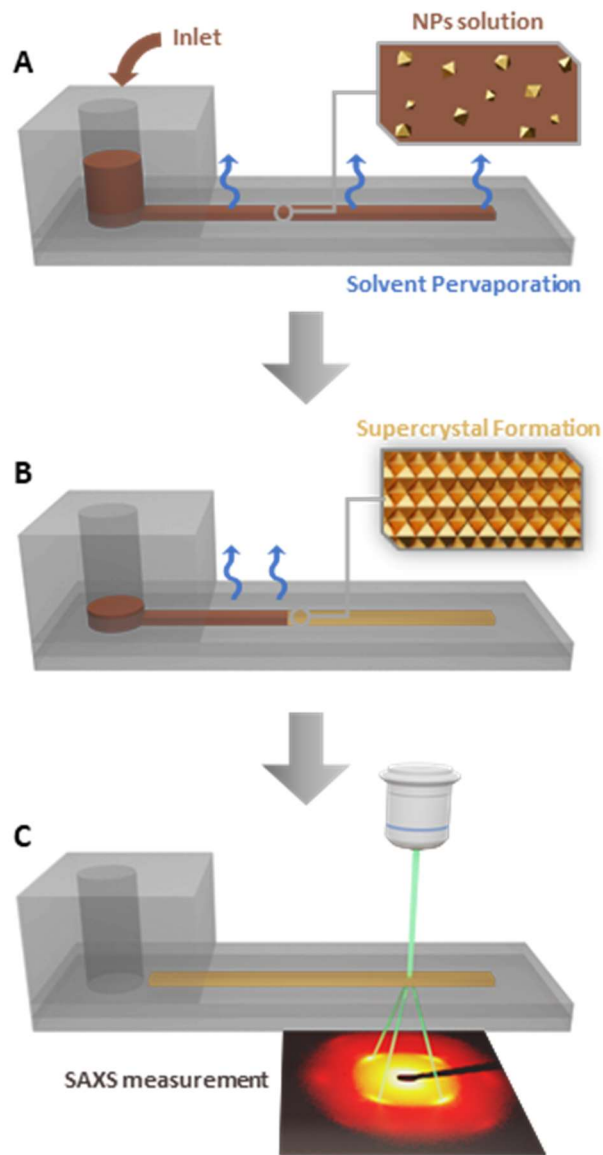
sample volumes have made the combination of SAXS and microfluidics quite challenging.<sup>[18]</sup> Moreover, the time-resolved analysis renders the problem even more complicated.

In this work, we analyze the organization of gold octahedra into single-domain supercrystals obtained by pervaporation within a microfluidic channel that spans millimeters. We use SAXS to investigate the orientation of the supercrystals over large scales and FIB-SEM tomography for local structural characterization in the real space. Interestingly, time-resolved SAXS revealed the crystallization dynamics of gold octahedra *in situ*. The results show single-domain supercrystals extending over the dimensions of the microfluidic channel (millimeters) that were oriented in a reproducible manner from sample to sample.

## Results and Discussion

Uniform Au octahedra with 4 different edge lengths were prepared by overgrowing single crystalline gold nanorods in the presence of butenoic acid.<sup>[13a]</sup> These samples were denoted as Oh<sub>*i*</sub>, where the subscript *i* indicates the mean edge length (in nm) of the octahedron: Oh<sub>53</sub>, Oh<sub>70</sub>, Oh<sub>75</sub>, and Oh<sub>85</sub>. The complete optical and structural characterization of the different particle batches by UV-Vis-NIR spectroscopy, transmission electron microscopy (TEM), and SAXS characterization is presented in the Supporting Information (**Figures S1-S4**). In SAXS, particle dimensions were determined by fitting the form factor obtained from the dilute colloid suspensions with a regular octahedron model (**Figure S5**). As shown in **Table S1**, the edge lengths obtained from SAXS for the different samples are in good agreement with those from TEM analysis. The standard deviation for the edge length was determined around 5-10% for all samples with both techniques.

The organization of Oh<sub>53</sub>, Oh<sub>70</sub>, Oh<sub>75</sub>, and Oh<sub>85</sub> into extended superlattices was carried out by pervaporation using a microfluidic device. As shown in **Scheme 1**, a concentrated dispersion of Au octahedra is pumped through the reservoir into a microchannel with a rectangular cross-section of 300 μm width, 25 μm height, and around 6 mm in length (see also **Scheme S1 in SI**).



**Scheme 1: Schematic representation of the preparation process of the Au supercrystal by pervaporation. (A)** A concentrated dispersion of Au octahedra is pumped within the microchannel and the solvent is allowed to evaporate through the thin PDMS membranes (pervaporation). **(B)** The pervaporation induces the accumulation of the Au octahedra at the end of the microchannel, inducing their crystallization and consequently the formation of a supercrystal. **(C)** *In situ* characterization by SAXS during the formation process of the Au supercrystals.

The solvent was allowed to evaporate through the thin PDMS films for at least 6 h. After complete solvent evaporation, the supercrystals were formed. The analysis of the optical properties of the resulting supercrystals showed low transmission and relatively high extinction (Figure S6). They were then studied in-house by *in situ* SAXS across the thin PDMS membranes. Regardless of the edge length of the octahedra, the assemblies exhibited discrete Bragg spots, indicating the presence of a single superlattice spanning areas larger than the footprint of the X-ray beam ( $300 \times 500 \mu\text{m}^2$ ) (Figure S7). We next performed *in situ* SAXS analysis on the SWING beamline of the SOLEIL synchrotron along the channel to determine the extension of the supercrystal (Figure 1).

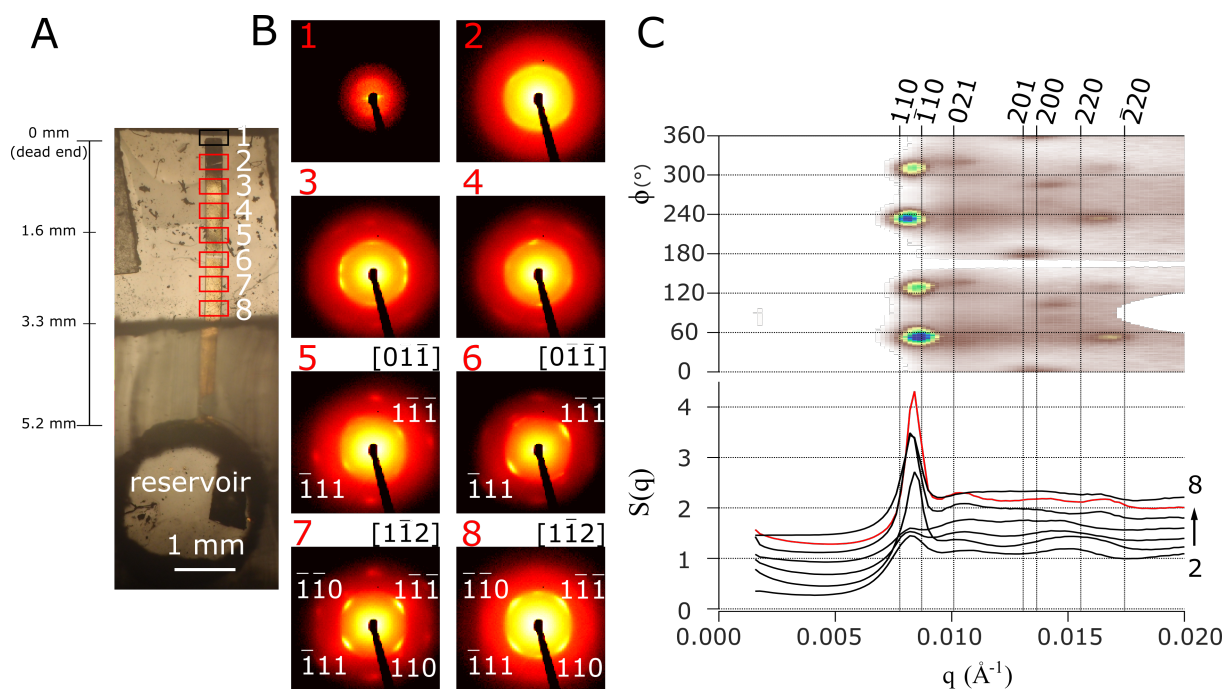


**Figure 1: *In-situ* space-resolved SAXS analysis of the gold octahedra supercrystal. (A)** Optical microscopy image of the microfluidic chip after the formation of the octahedra supercrystal. **(B)** Two-dimensional SAXS images acquired at different zones of the channel, indicated in (A) with numbered rectangles. Miller indices are indicated on some images for the strongest Bragg peaks together with the zone axis [UVW]. The dimension of the rectangles corresponds to the footprint of the X-Ray beam ( $300 \times 500 \mu\text{m}^2$ ). SAXS images are shown on

a logarithmic intensity scale. **(C)** (top) Angular distribution of the scattered intensity in position 7 and (bottom) structure factors of supercrystals obtained from position 2 to 8. Vertical lines indicate the expected positions of the Bragg peaks for the  $C/2m$  monoclinic space group. Measurements performed on Oh<sub>85</sub> at SWING.

Although the assemblies were polycrystalline at the beginning of the supercrystal (position 2, **Figure 1A** and **1B2**), as indicated by the ring-shaped scattering pattern, monodomains supercrystals were present hereafter (positions 4 to 8, **Figure 1A** and **Figure 1B3-8**), as evidenced by Bragg peaks on the two-dimensional SAXS images. The strongest Bragg peaks are indexed in **Figure 1B** using the  $C2/m$  monoclinic unit cell. The crystallographic orientation of the lattice is given by the zone axis (see **Figure 1B**), which corresponds to the direction of the crystal parallel to the X-ray beam. Remarkably, the (111) reflection is observed at the same position for all images from positions 5 to 8, showing that the monodomain supercrystal is covering at least  $1.7 \times 0.3 \text{ mm}^2$ . Its length is probably underestimated because we could not measure beyond position 8 since our microfluidic chips have a thick PDMS region with low X-Ray transmission, needed for the fabrication of the reservoir (**Figure 1A** and **Scheme 1**). To the best of our knowledge, this octahedron superlattice is among the largest single domain reported for plasmonic NPs to date. We also obtained the structure factor  $S(q)$  as the ratio between the intensity scattered by the supercrystal and the one for isolated Au nanoparticles. As shown in **Figure 1C**, the spectra recorded from position 2 to 8 exhibit Bragg peaks, which are in agreement with the  $C2/m$  monoclinic space group.

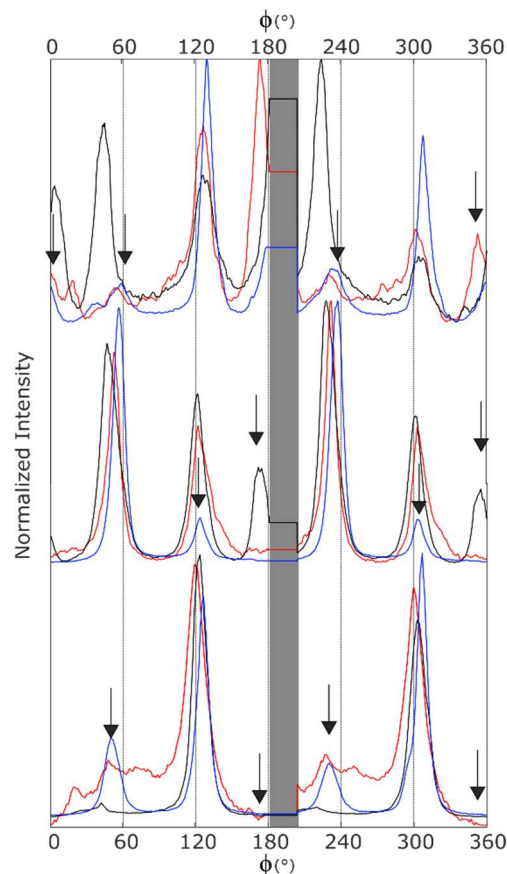


**Figure 2: Analysis of the supercrystal orientation.** Azimuthal integration at  $q=0.0083 \text{ \AA}^{-1}$  of the SAXS scattering from Oh<sub>85</sub> supercrystals over three channels (shifted vertically) at three different positions (labeled with different colors). The vertical grid with 60° spacing is a guide for the eye. Measurements performed on Oh<sub>85</sub> at SWING.

Finally, azimuthal integration of the SAXS images revealed that the supercrystals in different experiments all had very similar crystallographic orientations. The azimuthal integration at the  $q$  position of the strongest Bragg reflection is shown in **Figure 2**. The Bragg peaks always appear at the same angles, demonstrating that the crystallographic lattice is everywhere positioned with the  $c$  axis close to the direction of the X-ray beam. Besides, the partial extinction of some spots and the detection of out-of-plane reflections (**Figure 1C**, **Figure S8**) revealed that the supercrystal plane is not orthogonal to the X-Ray beam but slightly tilted,<sup>[19]</sup>

presumably due to the softness of the PDMS membrane leading to small deformations or curvatures (**Figure S9**). We emphasize that for well-ordered lattices even a very small tilt can bring the peaks out of the reflection condition, leading to almost complete extinction. This effect is much less visible when using a laboratory setup where the resolution is much lower and the patterns are quite symmetric (**Figure S10**). Note that this analysis was carried out for three different channels at three different positions (between 1.9 mm and 3.3 mm from the dead-end of the channel), confirming in all cases the presence of extended supercrystals oriented in the same direction. The curvature of the membrane is a consequence of its reduced thickness and this configuration is necessary for performing SAXS. It is noteworthy that we previously built the channels between one thin membrane and a thick PDMS slab, keeping the channel straight, for sensing applications.<sup>13</sup> The SAXS experiments, however, require a much thinner sample, since the X-rays would be absorbed by a thicker PDMS layer. Although the resulting membrane curvature complicates the analysis of the result, the crystallographic orientation analysis provides good estimates of the monodomain size.

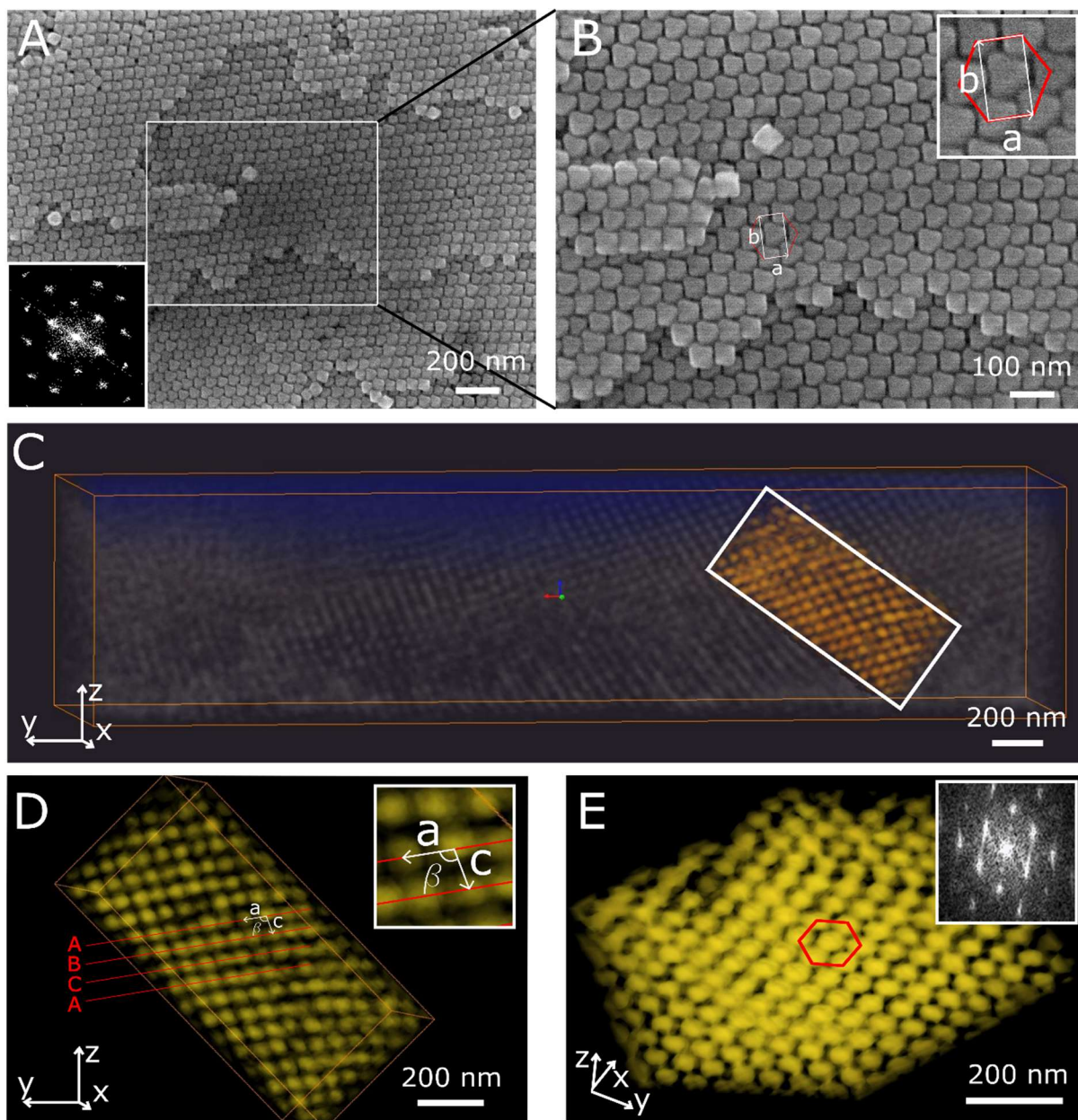


**Figure 3: SEM characterization of the Au supercrystal.** (A-B) SEM micrographs of the octahedra superlattice, viewed from the top. The inset in A is a Fast-Fourier transform (FFT) of the image and the inset in B shows the lattice parameters  $a$  and  $b$  of the monoclinic unit cell. (C) Three-dimensional reconstruction of a portion of the supercrystal. The blue color indicates the top of the supercrystal. The volume of the box is  $3.3 \times 0.8 \times 0.9 \mu\text{m}^3$ . (D-E) Magnified region of the supercrystal corresponding to the highlighted orange part in C, viewed in two different orientations. The Inset shows the lattice parameters  $a$ ,  $c$ , and  $\beta$  of the monoclinic unit cell. The

inset in E is the FFT of the corresponding image. The volume of the box is 720 x 340 x 500 nm<sup>3</sup>. Oh<sub>53</sub> were used in A-E.

In order to confirm the lattice structure, the nanostructuration was probed by SEM, revealing that the octahedra were ordered in monolayers with a hexagonal in-plane arrangement (**Figure 3A-B**). Fast-Fourier transform (FFT) analysis of the image confirmed this order by displaying 6 peaks arranged on a regular hexagon (inset in **Figure 3A**). The analysis also showed that within a monolayer, all octahedra were having the same orientation, with a triangular face parallel to the monolayers. All monolayers were identical and were stacked in a way such that a vertex of an octahedron in one monolayer touches the center of a particle edge in the neighboring monolayer (**Figure S11**). These observations are in agreement with the previously reported base-centered monoclinic packing.<sup>[2c]</sup> Further investigation of the internal structure was carried out by focused ion beam (FIB) in tandem with SEM imaging. This technique (Slice and View<sup>TM</sup> method) allows 3D rendering of a portion of the supercrystal (**Figure 3C-E, Video 1 Supporting Information**).<sup>[20]</sup> The hexagonal monolayers were stacked in an ABC fashion, with a relative offset of one layer to the next of 1/3 along the **c** monoclinic lattice vector direction, confirming the monoclinic packing of the octahedra (**Figure 3D**). Based on these observations we confirm that the supercrystal belongs to the C2/m space group, in agreement with the SAXS analysis. Indeed, the monoclinic lattice is face-centered and there is a mirror plane in the (**a,c**) plane and a two-fold axis perpendicular to this mirror plane (**Figure S11**). Additional projections of the 3D supercrystal region are shown in the supporting information (**Figure S12**). The other lattice polymorphs (i.e. simple hexagonal and Minkowski) were not observed.

Interestingly, the results obtained indicate that there is no effect of the particle size on the superlattice formation. Therefore, considering a monoclinic lattice packing and a channel height of 25 μm, it is possible to estimate the number of layers in the supercrystal by correlating the

edge length of the octahedron with the distance between monolayers (see **Figure S11**), which can be described as  $d_{layer} = \sqrt{3}/2 \cdot a_{octa}$ . Therefore, the estimated number of nanoparticle layers within a supercrystal varied between 328 and 545 for octahedra with edge lengths from 85 to 53 nm.

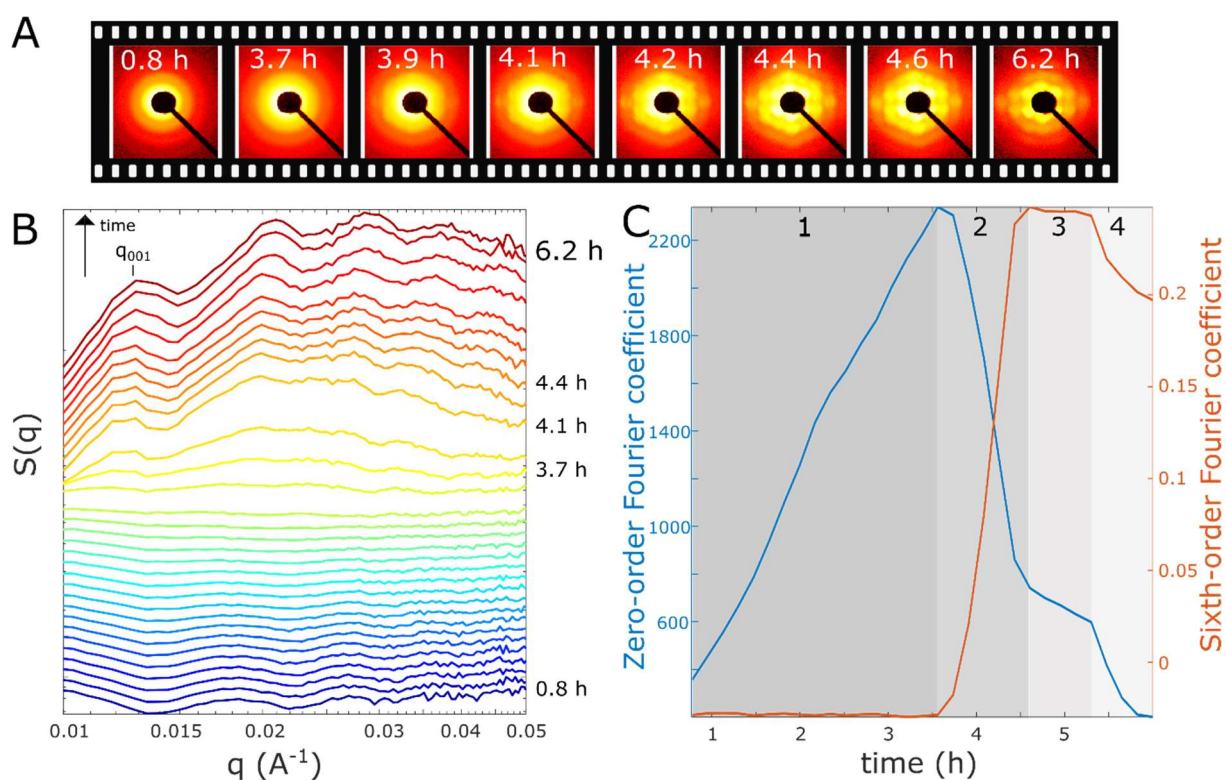


**Figure 4: Time-resolved SAXS of the supercrystal formation.** (A) Two-dimensional SAXS images taken at a fixed position in the middle of the channel at different times. The time was measured from particle infiltration until complete evaporation. (B) Corresponding structure factor measured every 12 min. (C) Zero- and sixth-order Fourier coefficient at the position of the first Bragg peak (blue and orange respectively). Grey shaded areas indicate four important stages during the supercrystal formation: (1) accumulation of nanoparticles, (2) nucleation and growth, (3) steady state, and (4) microchannel drying. These measurements were performed in-house on the Oh<sub>75</sub> sample.

The formation kinetics of the supercrystal were investigated by time-resolved *in situ* SAXS (**Figure 4**). Two-dimensional SAXS images were recorded at a fixed position in the middle of the channel every 12 min until complete solvent evaporation (**Figure 4A**). Moreover, from the SAXS images we obtained the time-resolved structure factor (**Figure 4B**) and the time-resolved zero-order and sixth-order coefficients at the position of the first Bragg peak (**Figure 4C**). While the zero-order coefficient is simply the average intensity (related to the particle concentration), the sixth-order coefficient corresponds to the 6<sup>th</sup> harmonic of the intensity peak normalized to the zero-order one and thus encodes the contrast of the 6 Bragg peaks (**Figure S13**). As shown in **Figure 4A**, the initial stage of the pervaporation process is characterized by a featureless scattering pattern, due to the form factor of the non-interacting octahedra. The particle concentration increases in the channel as evaporation progresses, resulting in the gradual increase of the form factor intensity rings (stage 1, **Figure 4C**). This process continued until a structure factor emerged, marking the onset of superlattice formation (stage 2, **Figure 4B-C**). The lattice then grew over 1h, with gradually reinforced Bragg peaks. A steady state was then observed (stage 3, **Figure 4B**), indicating the supercrystal growth arrest. In the final stage of the drying process, the intensity drops slightly (stage 4, **Figure 4C**), presumably due to capillary forces dragging away a small portion of the supercrystal. The evolution of the SAXS pattern along with its analysis is provided in **Video 2** in the Supporting Information and shows that the orientation of the lattice did not vary over time. Overall, the supercrystal forms *via* two consecutive processes: (1) gradual concentration of the colloids followed by (2) nucleation and growth of the supercrystal.

We next compared the organization obtained by pervaporation with a more standard EISA process, drop-casting, using the same dispersion of gold octahedra (see the Experimental Section for details). In this configuration, only diffuse scattering was detected (**Figure S14**),

showing the absence of an ordered lattice. Clearly, the closed microfluidic environment is important for obtaining extended superlattices. In a drop-casting experiment, particles accumulate at the drying front due to the coffee-ring effect,<sup>[21]</sup> where capillary forces at the air/liquid interface play an important role in the arrangement of the NPs and lead to a disordered deposit. In the pervaporation configuration, the suppression of capillary effects during self-organization likely leads to the formation of a single supercrystal inside the microfluidic channels. Moreover, pervaporation generates a solvent flux from the reservoir toward the channel, resulting in NPs accumulation and favoring crystallization (stage 1, **Figure 4C**). Gravitational sedimentation can be neglected, as a similar organization was noticed whether the chip was placed horizontally or vertically during the pervaporation process (**Figure S15**). The reproducible orientation of the supercrystal in different channels can hardly be a confinement-related effect since the channel width exceeds the NP size by more than two orders of magnitude. As shown in **Figure 4A**, the orientation of the supercrystal does not vary during the growth stage, suggesting that the nucleation and growth of the supercrystal were directed by the PDMS walls.

Finally, the pervaporation-induced self-assembly of other types of particles, i.e. gold spheres (with diameter  $42.0 \pm 3.0$  nm) and nanorods (with length  $49.4 \pm 4.7$  nm and width  $12.3 \pm 1.8$  nm) were investigated (**Figure S16**). In a similar way to octahedra, gold spheres were found to assemble into single supercrystals (**Figure S16A**). In contrast, the SAXS patterns of rod samples exhibit well-defined rings, revealing multi-domain (powder) supercrystals (**Figure S16B**). These experiments show the potential application of pervaporation to assembling other NP shapes.

## Conclusion

SAXS analysis of the self-assembly of gold octahedra by pervaporation in a microfluidic channel revealed the formation of single-domain supercrystals. To the best of our knowledge,

the size of the supercrystals is among the largest reported to date for plasmonic NPs. Supercrystal analysis by SAXS and FIB-SEM tomography indicated the formation of extended superlattices with a monoclinic  $C/2m$  crystalline symmetry. Supercrystal formation was also investigated by time-resolved *in situ* SAXS, revealing a multistep formation process, with an initial accumulation stage when the nanoparticles concentrated in the channel, followed by nucleation and crystal growth. Moreover, we found that the orientation of the supercrystal did not change during the growth, leading to a single-domain supercrystal, which ultimately adopted the shape of the microfluidic channel. This pervaporation approach favored the formation of the monoclinic lattice at the expense of the other polymorphs usually observed by alternative EISA approaches. Thus, we demonstrate that the self-assembly process leads to the formation of large single-domain supercrystals with potential plasmonics and optics applications for analytical chemistry.

## Experimental Section

**Materials.** L-ascorbic acid ( $\geq 99\%$ ), sodium borohydride ( $\text{NaBH}_4$ ,  $99\%$ ), 3-butenoic acid ( $\text{C}_3\text{H}_6\text{O}_2$ ,  $97\%$ ), hexadecyltrimethylammonium bromide (CTAB,  $\geq 96\%$ ) and sodium chloride ( $\text{NaCl}$ ,  $99\%$ ) were purchased from Sigma-Aldrich. Hydrochloric acid ( $\text{HCl}$ ,  $37\%$ ) was supplied by Scharlab. Tetrachloroauric (III) acid trihydrate ( $\text{HAuCl}_4 \cdot 3\text{H}_2\text{O}$ ,  $99.9\%$ ) was supplied by Alfa-Aesar, silver nitrate ( $\text{AgNO}_3$ ,  $\geq 99.9\%$ ) by Stream Chemicals, and poly(dimethylsiloxane) (PDMS, Sylgard-184) by Dow-Corning. All chemicals were used without further purification. Milli-Q grade water was used in synthesis.

**Synthesis of Gold nanorods.** Gold nanorods were prepared by the seed-mediated growth method as previously reported.<sup>[22]</sup> The standard procedure consisted in the preparation of a fresh dispersion of Au seed by quick addition of a freshly prepared  $\text{NaBH}_4$  ( $300\ \mu\text{L}$ ,  $0.1\ \text{M}$ ) solution to an aqueous mixture of  $4.7\ \text{mL}$  of  $0.1\ \text{M}$  CTAB and  $25\ \mu\text{L}$  of  $0.05\ \text{M}$   $\text{HAuCl}_4$  under vigorous

stirring for 5 min. The dispersion was kept undisturbed at 27 °C for 1 h. Then, 625  $\mu$ L of the seed dispersion was added to 250 mL of a growth solution containing 0.1 M CTAB, 0.5 mM HAuCl<sub>4</sub>, 0.12 mM AgNO<sub>3</sub>, 10 mM HCl, and 0.8 mM ascorbic acid and kept at 27 °C overnight. Gold nanorods with a longitudinal surface plasmon resonance at 846 nm were obtained and purified by two rounds of centrifugation (8500 rpm, 25 min). The purified nanorods (**Figure S17**) were redispersed in 1 mM CTAB solution to a final concentration of 200 mM in terms of Au<sup>0</sup>.

**Synthesis of Gold Octahedra.** Gold octahedra were prepared as previously reported.<sup>[13a]</sup> This synthesis involved the use of the Au nanorods as seeds and their subsequent overgrowth. A growth solution was constituted by mixing 422  $\mu$ L of 3-butenic acid (11.77 M) to 100 mL of an aqueous mixture containing 0.5 mM HAuCl<sub>4</sub> and 10 mM CTAB at 60 °C. The solution changed from orange to colourless in 3 min, indicating the reduction of Au<sup>+3</sup> species to Au<sup>+</sup>. Then, a certain volume of the purified gold nanorods (2.0 mM in terms of Au<sup>0</sup>) was added as seed and the mixture was kept at 60 °C for 6 h. The volume of seed solution determines the final size of the gold octahedra (see **Figure S1-4** and **Table S1**). Finally, the NPs were washed by two rounds of centrifugation (3000 rpm, 30 min) and the pellet was redispersed in 1 mM CTAC to a final Au<sup>0</sup> concentration of 200 mM.

**Synthesis of Gold Spheres.** Gold nanospheres were prepared following a seeded-growth method previously reported by Rodríguez-Fernández et al.<sup>[23]</sup> First, 14 nm citrate-stabilized gold seeds were prepared following the protocol described by Turkevich et al.<sup>[24]</sup> followed by a centrifugation and redispersion cycle ([Au]= 2 mM in terms of Au<sup>0</sup>). Subsequently, gold seeds were overgrown by adding 5 mL into a growth solution (250 mL) containing HAuCl<sub>4</sub> 1mM, CTAB 15 mM, and ascorbic acid 2 mM at 30 °C and letting it react for 2h. The resulting nanoparticle dispersion is a mix of gold spheres, nanorods, and planar shapes. Gold spheres were purified by depletion forces.<sup>[25]</sup> The as-prepared nanoparticles were centrifuged (3500 rpm

x 30 min) and redispersed in 180 mM CTAC to obtain a final Au<sup>0</sup> concentration of 5 mM. The solution remained undisturbed for 6 h. After which the supernatant (containing gold spheres) was separated and centrifuged to obtain a concentrated dispersion of purified gold nanospheres (**Figure S18**) containing an Au<sup>0</sup> concentration of 200 mM and 1mM CTAB.

***Fabrication of the microfluidic chips.*** Microfluidic chips were prepared by standard soft lithography techniques.<sup>[26]</sup> The channels were 300 μm in width, 25 μm in height and 6 mm in length. A schematic description of this process is available in **Scheme S1 in SI**. 6 mL of a mixture of PDMS monomers and curing agent (10:1 w/w) was poured on the silicon wafer and spin-coated at 2500 rpm during 10 s with acceleration and deceleration of 500 rpm/s to obtain a thin PDMS film of ≈ 75 μm covering the SU-8 resin features. Then the film was cured at 60 °C for 2 h. At the same time, a 5 mm thick PDMS slab was prepared, cured for 2 h at 60 °C and then cut in a rectangular piece of 7 x 3 cm<sup>2</sup> with a central hole of 5 x 1 cm<sup>2</sup>. The two PDMS parts were exposed to an oxygen plasma (8 sccm (standard cubic centimeters per minute) of O<sub>2</sub> and 40 sccm of Ar, 65 W, and 20 s) after which they were sealed together. In order to enhance adhesion, the chip was heated at 100 °C for 10 min. Finally, the chip was punched to make an inlet and bonded to another thin PDMS film (≈75 μm), prepared as previously described but without any template, to close the microfluidic channels.

***Formation of Au supercrystals within the microfluidic chip.*** 20 μL of a highly concentrated dispersion of gold octahedra ([Au<sup>0</sup>] ≈ 0.2 M) was injected inside the microfluidic chip. Positive pressure was then applied on the inlet to fill the channel, either with a microfluidic pump (250 mbar) for 30 min or manually with a syringe pump. The dispersion was allowed to dry by pervaporation in ambient conditions.

***SAXS experiments.*** The supercrystal structures were probed by SAXS at the Laboratoire de Physique des Solides (LPS) and at the SOLEIL Synchrotron. Two-dimensional data reduction was done using the *Nika* software implemented in *Igor Pro*.<sup>[27]</sup> SAXS data in Figure 4 were

collected at LPS using a rotating anode (Cu K $\alpha$ ,  $\lambda = 0.154$  nm) and the chip was oriented vertically in order to place the microchannel at normal incidence in respect of the beam. The beam size on the sample was about  $0.5 \times 0.5$  mm<sup>2</sup>. The scattered X-rays were collected on a Pilatus 200K detector (Dectris Ltd, Switzerland) with pixel size 172  $\mu$ m. The sample – detector distance was 1.392 m. Exposure times were typically around 3.5 minutes. The SAXS data in Figures 1 and 2 were collected at the SWING beamline of the SOLEIL synchrotron (Saint-Aubin, France), at a beam energy of 12 keV and a sample-to-detector distance of 6.376 m. The scattered signal was recorded by an Eiger 4 M detector (Dectris Ltd, Switzerland) with pixel size 75  $\mu$ m. The beam size on the sample was about  $0.5 \times 0.3$  mm<sup>2</sup>. Exposure times were around 50 ms. Form factor analysis using SAXS on dilute suspensions (**Figure S5**) was done using the SasView software ([www.sasview.org](http://www.sasview.org)) with a dedicated plugin model for the octahedron shape. The model description and code are available at <http://marketplace.sasview.org/models/134/>. The two-dimensional SAXS images were analyzed using Crystal Maker software.

**Nanoparticles Characterization.** UV-Vis-NIR extinction spectra were acquired using a Cary 8454 spectrophotometer (Agilent) in quartz cuvettes (1 cm optical path length). Transmission electron microscopy (TEM) images were obtained with a JEOL JEM 1010 microscope operating at an acceleration voltage of 100 kV. Optical characterization of the supercrystals was performed with a BRUKER FTIR spectrometer (Vertex 70) attached to an optical microscope (Hyperion 2000) using a 4x objective (NA 0.1) and a spatial mask.

**FIB-SEM tomography.** To perform scanning electron microscopy (SEM) characterization, the supercrystal must be extracted from the channel. For this reason, the microfluidic chip was not subjected to the oxygen plasma to avoid irreversible bonding. Before SEM observation, a plasma treatment (H<sub>2</sub> 6.4 sccm, Ar 27.5 sccm, 50 W during 2 min, Gatan Model 955) was performed to remove organic molecules from the supercrystal surface. FIB-SEM tomography of the supercrystal was performed in a Helios Nanolab 450 FIB-SEM (Thermo Fisher

Scientific). After defining the area of interest, a standard preparation protocol was followed: deposition of a  $\sim 1 \mu\text{m}$  Pt protective layer (starting with electron beam-induced deposition to prevent surface damage and followed by ion beam-induced deposition), trenches were milled around the examined volume and the cross-section was polished to reveal the structure and perform a final optimization of imaging conditions in the electron beam. Slicing was then performed with the ion beam at an accelerating voltage of 30 kV and a beam current of 24 pA. After each FIB cut, an electron image was acquired using the high-resolution mode at 5kV and 25 pA. The resulting image has a field of view of  $3.3 \times 2.2 \mu\text{m}$  at  $1536 \times 1024$  px resolution, which corresponds to a pixel size of  $2.16 \times 2.16 \text{ nm}^2$ . A series of 110 slices were acquired with a target slice thickness of 8 nm. Further data processing, including alignment, filtration, and visualization were performed using the Aviso 8.1 software (Thermo Fisher).

### **Acknowledgements**

The CNRS is acknowledged for funding and support. This work was supported by the Ministerio de Economía y Competitividad (MINECO, Spain, grants: MAT2016-77809-R and PID2019-108954RB-100), Xunta de Galicia/FEDER (grant GRC ED431C 2016-048), and has benefited from an Investissements d'Avenir grant from Labex PALM (ANR-10-LABX-0039-PALM). D. G.-L. and S.G.-G. acknowledge MINECO for a predoctoral scholarship (FPI, BES-2017-081670) and postdoctoral grant (Juan de la Cierva, IJCI-2016-29108), respectively. We acknowledge SOLEIL for the provision of synchrotron radiation facilities, and we thank Thomas Bizien for assistance in using beamline SWING. Alexandra Beikert is acknowledged for implementing the octahedron model as a SasView plugin. Dr. Agustín Mihi and Dr. Nicolás Passarelli are thanked for measuring the optical properties of the supercrystals.

### **References**

- [1] a) N. Vogel, M. Retsch, C. A. Fustin, A. Del Campo, U. Jonas, *Chem. Rev.* **2015**, *115*, 6265; b) K. Thorkelsson, P. Bai, T. Xu, *Nano Today* **2015**, *10*, 48; c) S. W. Hsu, A. L. Rodarte, M. Som, G. Arya, A. R. Tao, *Chem. Rev.* **2018**, *118*, 3100; d) K. Deng, Z. Luo, L. Tan, Z. Quan, *Chem. Soc. Rev.* **2020**, *49*, 6002; e) D. Garcia-Lojo, S. Nunez-Sanchez, S. Gomez-Grana, M. Grzelczak, I. Pastoriza-Santos, J. Perez-Juste, L. M. Liz-Marzan, *Acc. Chem. Res.* **2019**, *52*, 1855.
- [2] a) X. Bouju, É. Duguet, F. Gauffre, C. R. Henry, M. L. Kahn, P. Mélinon, S. Ravaine, *Adv. Mater.* **2018**, *30*, 1706558; b) K. L. Young, M. L. Personick, M. Engel, P. F. Damasceno, S. N. Barnaby, R. Bleher, T. Li, S. C. Glotzer, B. Lee, C. A. Mirkin, *Angew. Chem. Int. Ed.* **2013**, *52*, 13980; c) J. Gong, R. S. Newman, M. Engel, M. Zhao, F. Bian, S. C. Glotzer, Z. Tang, *Nat. Commun.* **2017**, *8*, 14038; d) P. F. Damasceno, M. Engel, S. C. Glotzer, *Science* **2012**, *337*, 453; e) C. Hamon, C. Goldmann, D. Constantin, *Nanoscale* **2018**, *10*, 18362; f) S. Torquato, Y. Jiao, *Nature* **2009**, *460*, 876; g) M. H. Huang, S. Thoka, *Nano Today* **2015**, *10*, 81; h) Z. Quan, J. Fang, *Nano Today* **2010**, *5*, 390.
- [3] S. Xie, X. Zhou, X. Han, Q. Kuang, M. Jin, Y. Jiang, Z. Xie, L. Zheng, *J. Phys. Chem. C* **2009**, *113*, 19107.
- [4] C.-C. Chang, H.-L. Wu, C.-H. Kuo, M. H. Huang, *Chem. Mater.* **2008**, *20*, 7570.
- [5] J. Henzie, M. Grünwald, A. Widmer-Cooper, P. L. Geissler, P. Yang, *Nat. Mater.* **2012**, *11*, 131.
- [6] Y. H. Lee, C. L. Lay, W. Shi, H. K. Lee, Y. Yang, S. Li, X. Y. Ling, *Nat. Commun.* **2018**, *9*, 2769.
- [7] W. Lu, Q. Liu, Z. Sun, J. He, C. Ezeolu, J. Fang, *J. Am. Chem. Soc.* **2008**, *130*, 6983.

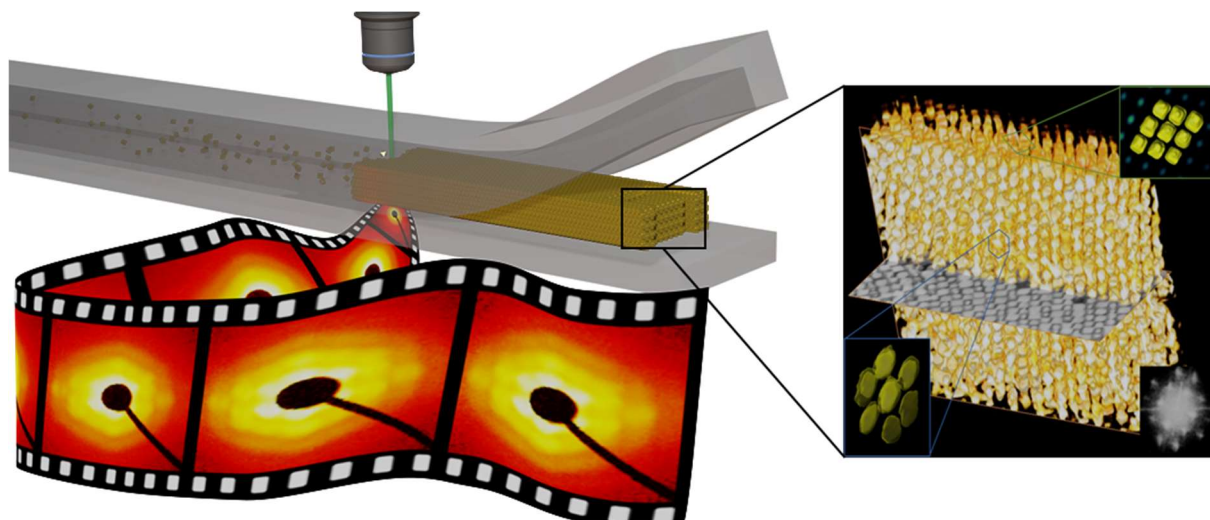
- [8] a) R. Li, J. Zhang, R. Tan, F. Gerdes, Z. Luo, H. Xu, J. A. Hollingsworth, C. Klinke, O. Chen, Z. Wang, *Nano Lett.* **2016**, *16*, 2792; b) J. Zhang, Z. Luo, Z. Quan, Y. Wang, A. Kumbhar, D.-M. Smilgies, J. Fang, *Nano Lett.* **2011**, *11*, 2912.
- [9] J. Zhang, Z. Luo, B. Martens, Z. Quan, A. Kumbhar, N. Porter, Y. Wang, D.-M. Smilgies, J. Fang, *J. Am. Chem. Soc.* **2012**, *134*, 14043.
- [10] M. A. Boles, M. Engel, D. V. Talapin, *Chem. Rev.* **2016**, *116*, 11220.
- [11] Y. H. Lee, W. Shi, H. K. Lee, R. Jiang, I. Y. Phang, Y. Cui, L. Isa, Y. Yang, J. Wang, S. Li, X. Y. Ling, *Nat. Commun.* **2015**, *6*, 6990.
- [12] a) C. W. Liao, Y. S. Lin, K. Chanda, Y. F. Song, M. H. Huang, *J. Am. Chem. Soc.* **2013**, *135*, 2684; b) C.-Y. Chiu, C.-K. Chen, C.-W. Chang, U. S. Jeng, C.-S. Tan, C.-W. Yang, L.-J. Chen, T.-J. Yen, M. H. Huang, *J. Am. Chem. Soc.* **2015**, *137*, 2265.
- [13] a) S. Gómez-Graña, C. Fernández-López, L. Polavarapu, J.-B. Salmon, J. Leng, I. Pastoriza-Santos, J. Pérez-Juste, *Chem. Mater.* **2015**, *27*, 8310; b) D. García-Lojo, S. Gómez-Graña, V. F. Martín, D. M. Solís, J. M. Taboada, J. Pérez-Juste, I. Pastoriza-Santos, *ACS Appl. Mater. Int.* **2020**, *12*, 46557.
- [14] a) J. Leng, B. Lonetti, P. Tabeling, M. Joanicot, A. Ajdari, *Phys. Rev. Lett.* **2006**, *96*, 084503; b) A. Merlin, J.-B. Salmon, J. Leng, *Soft Matter* **2012**, *8*, 3526; c) J. Leng, J.-B. Salmon, *Lab Chip* **2009**, *9*, 24.
- [15] a) J. Angly, A. Iazzolino, J.-B. Salmon, J. Leng, S. P. Chandran, V. Ponsinet, A. Désert, A. Le Beulze, S. Mornet, M. Tréguer-Delapierre, M. A. Correa-Duarte, *ACS Nano* **2013**, *7*, 6465; b) P. Massé, S. Mornet, E. Duguet, M. Tréguer-Delapierre, S. Ravaine, A. Iazzolino, J. B. Salmon, J. Leng, *Langmuir* **2013**, *29*, 1790.
- [16] a) F. Schulz, O. Pavelka, F. Lehmkuhler, F. Westermeier, Y. Okamura, N. S. Mueller, S. Reich, H. Lange, *Nat. Commun.* **2020**, *11*, 3821; b) B. Abécassis, F. Testard, O. Spalla, *Phys. Rev. Lett.* **2008**, *100*, 115504; c) P.-W. Yang, S. Thoka, P.-C. Lin, C.-J.

- Su, H.-S. Sheu, M. H. Huang, U. S. Jeng, *Langmuir* **2017**, *33*, 3253; d) F. Montanarella, J. J. Geuchies, T. Dasgupta, P. T. Prins, C. van Overbeek, R. Dattani, P. Baesjou, M. Dijkstra, A. V. Petukhov, A. van Blaaderen, D. Vanmaekelbergh, *Nano Lett.* **2018**, *18*, 3675.
- [17] a) Y. Yu, D. Yu, B. Sadigh, C. A. Orme, *Nat. Commun.* **2018**, *9*, 4211; b) S. Connolly, S. Fullam, B. Korgel, D. Fitzmaurice, *J. Am. Chem. Soc.* **1998**, *120*, 2969; c) S. Narayanan, J. Wang, X.-M. Lin, *Phys. Rev. Lett.* **2004**, *93*, 135503; d) I. Lokteva, M. Koof, M. Walther, G. Grübel, F. Lehmkuhler, *J. Phys. Chem. Lett.* **2019**, *10*, 6331.
- [18] a) K. N. Toft, B. Vestergaard, S. S. Nielsen, D. Snakenborg, M. G. Jeppesen, J. K. Jacobsen, L. Arleth, J. P. Kutter, *Anal. Chem.* **2008**, *80*, 3648; b) V. Lutz-Bueno, J. Zhao, R. Mezzenga, T. Pfohl, P. Fischer, M. Liebi, *Lab Chip* **2016**, *16*, 4028; c) S. Merkens, M. Vakili, A. Sánchez-Iglesias, L. Litti, Y. Gao, P. V. Gwozdz, L. Sharpnack, R. H. Blick, L. M. Liz-Marzán, M. Grzelczak, M. Trebbin, *ACS Nano* **2019**, *13*, 6596.
- [19] A. V. Petukhov, J.-M. Meijer, G. J. Vroege, *Curr. Opin. Colloid Interface Sci.* **2015**, *20*, 272.
- [20] C. Hamon, M. N. Sanz-Ortiz, E. Modin, E. H. Hill, L. Scarabelli, A. Chuvilin, L. M. Liz-Marzan, *Nanoscale* **2016**, *8*, 7914.
- [21] R. D. Deegan, O. Bakajin, T. F. Dupont, G. Huber, S. R. Nagel, T. A. Witten, *Nature* **1997**, *389*, 827.
- [22] B. Nikoobakht, M. A. El-Sayed, *Chem. Mater.* **2003**, *15*, 1957.
- [23] J. Rodríguez-Fernández, J. Pérez-Juste, F. J. García de Abajo, L. M. Liz-Marzán, *Langmuir* **2006**, *22*, 7007.
- [24] J. Turkevich, P. C. Stevenson, J. Hillier, *Discuss. Faraday Soc.* **1951**, 55.
- [25] N. R. Jana, *Chem. Commun.* **2003**, 1950.

[26] D. Qin, Y. N. Xia, G. M. Whitesides, *Nat. Protoc.* **2010**, 5, 491.

[27] J. Ilavsky, *J. Appl. Crystallogr.* **2012**, 45, 324.

## TOC



A pervaporation-induced self-assembly strategy is used to obtain supercrystals of gold octahedra in a microfluidic channel. Supercrystal analysis by SAXS and FIB-SEM tomography indicates the formation of extended superlattices with a monoclinic  $C/2m$  crystalline symmetry. The size of the supercrystals is among the largest reported to date for plasmonic NPs covering at least  $1.7 \times 0.3 \text{ mm}^2$ .